
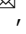








## Low-temperature hysteresis broadening emerging from domain-wall creep dynamics in a two-phase competing system

Keisuke Matsuura <sup>1,8</sup>, Yo Nishizawa<sup>2</sup>, Yuto Kinoshita<sup>3</sup>, Takashi Kurumaji<sup>4</sup>, Atsushi Miyake <sup>3</sup>, Hiroshi Oike <sup>1,2,5</sup>, Masashi Tokunaga <sup>1,3</sup>, Yoshinori Tokura <sup>1,2,6</sup> & Fumitaka Kagawa <sup>1,2,7</sup>

Hysteretic behaviour accompanies any first-order phase transition, forming a basis for many applications. However, its quantitative understanding remains challenging, and even a qualitative understanding of pronounced hysteresis broadening at low temperature, which is often observed in magnetic-field-induced first-order phase transition materials, is unclear. Here, we show that such pronounced hysteresis broadening emerges if the phase-front velocity during the first-order phase transition exhibits an activated behaviour as a function of both temperature and magnetic field. This is demonstrated by using real-space magnetic imaging techniques, for the magnetic-field-induced first-order phase transition between antiferromagnetic and ferrimagnetic phases in  $(\text{Fe}_{0.95}\text{Zn}_{0.05})_2\text{Mo}_3\text{O}_8$ . When combined with the Kolmogorov-Avrami-Ishibashi model, the observed activated temperature- and field-dependences of the growth velocity of the emerging antiferromagnetic domain quantitatively reproduce the pronounced hysteresis broadening. Furthermore, the same approach also reproduces the field-sweep-rate dependence of the transition field observed in the experiment. Our findings thus provide a quantitative and comprehensive understanding of pronounced hysteresis broadening from the microscopic perspective of domain growth.

<sup>1</sup>RIKEN Center for Emergent Matter Science, Wako 351-0198, Japan. <sup>2</sup>Department of Applied Physics and Quantum-Phase Electronics Center (QPEC), University of Tokyo, Tokyo 113-8656, Japan. <sup>3</sup>The Institute for Solid State Physics, The University of Tokyo, Kashiwa, Chiba 277-8581, Japan. <sup>4</sup>Department of Advanced Materials Science, The University of Tokyo, Kashiwa 277-8561, Japan. <sup>5</sup>PRESTO, Japan Science and Technology Agency (JST), Kawaguchi 332-0012, Japan. <sup>6</sup>Tokyo College, University of Tokyo, Tokyo 113-8656, Japan. <sup>7</sup>Department of Physics, Tokyo Institute of Technology, Tokyo 152-8551, Japan. <sup>8</sup>Present address: Department of Physics, Tokyo Institute of Technology, Tokyo 152-8551, Japan. ✉email: [matsuura@phys.titech.ac.jp](mailto:matsuura@phys.titech.ac.jp); [kagawa@phys.titech.ac.jp](mailto:kagawa@phys.titech.ac.jp)

Functionalities carried by ferroic materials are closely related to their hysteretic behavior that accompanies the first-order phase transition (FOT) associated with the order parameter reversal. Ferromagnets or ferroelectric materials with a high coercive magnetic or electric field facilitate a remnant order parameter; these materials have been applied to permanent magnets<sup>1</sup>, piezo elements<sup>2</sup>, and recording media<sup>3,4</sup>. Alternatively, those materials with a low coercive field have superior sensitivity and switching ability<sup>5</sup> have been applied to motors, capacitors, transformers, and power supplies. In addition to these commercial products, the hysteretic behavior accompanying a field-induced FOT between competing phases with different symmetries plays a key role in exotic functionalities, such as nonvolatile resistance control by a magnetic field<sup>6,7</sup> and magneto- or electrocaloric refrigeration<sup>8</sup>. From a microscopic viewpoint, hysteretic behavior accompanying an FOT originates from the nonequilibrium evolution dynamics of the emerging phase, such as nucleation and growth; thus, the hysteretic behavior tends to vary with the sweep rate of relevant parameters, also dictating the performance under high-speed operation<sup>9</sup>.

For a field-induced FOT in a single-crystalline sample, the transition profile is usually sharp, and accordingly, two characteristic transition fields,  $H_{\text{high}}^*$  and  $H_{\text{low}}^*$ , can be defined: one is higher than the field of the equilibrium FOT,  $H_c$ , and the other is lower. Thus, by plotting  $H_{\text{high}}^*$  and  $H_{\text{low}}^*$  at various temperatures, two hysteresis lines,  $H_{\text{high}}^*(T)$  and  $H_{\text{low}}^*(T)$ , sandwiching the equilibrium FOT line,  $H_c(T)$ , can be drawn in the phase diagram. However, in some materials exhibiting a magnetic field-induced FOT, the difference between  $H_{\text{high}}^*(T)$  and  $H_{\text{low}}^*(T)$ , i.e., the hysteresis width, starts to increase below a certain temperature and eventually shows a large hysteresis width of more than several Tesla at low temperatures. For example, the hysteresis width between ferrimagnetic up and down states in multiferroic  $\text{LuFe}_2\text{O}_4$  reaches  $\sim 18$  T at 4.2 K<sup>10</sup>. Although it is rare for ferroic materials to exhibit such high coercivity, there are many examples of field-induced FOTs between competing phases of different symmetries that exhibit pronounced hysteresis broadening toward low temperatures (Fig. 1a), for instance, the colossal magnetoresistive manganite<sup>6</sup>,  $\text{Gd}_5\text{Ge}_4$ <sup>11</sup>,  $\text{LaFe}_{12}\text{B}_6$ <sup>12</sup>, doped  $\text{CeFe}_2$  alloy<sup>13</sup>, and doped  $\text{Mn}_2\text{Sb}$ <sup>14,15</sup>. Similar hysteresis broadening has also been observed for a structural FOT in martensitic materials<sup>16,17</sup> and aqueous solutions<sup>18</sup>, implying that common physics, which is not limited to magnetic materials, underlies these observations. However, different equations have been used for different systems to analyze hysteresis lines<sup>10,16,17,19–21</sup>, and thus, the universal relationship between microscopic domain-wall motion and the broadening of hysteresis lines at low temperature remains unclear. Such hysteresis broadening is also potentially relevant to thermal-quenching-induced metastable states in quantum materials<sup>22</sup>. For example,  $\text{IrTe}_2$  exhibits a metastable superconducting state when thermal quenching is applied<sup>23</sup>. This behavior can be understood by assuming the hysteresis broadening accompanying the chemical-doping-induced FOT, although it is not possible to demonstrate directly the hypothetical broadening in this system by continuously changing the composition at low temperatures.

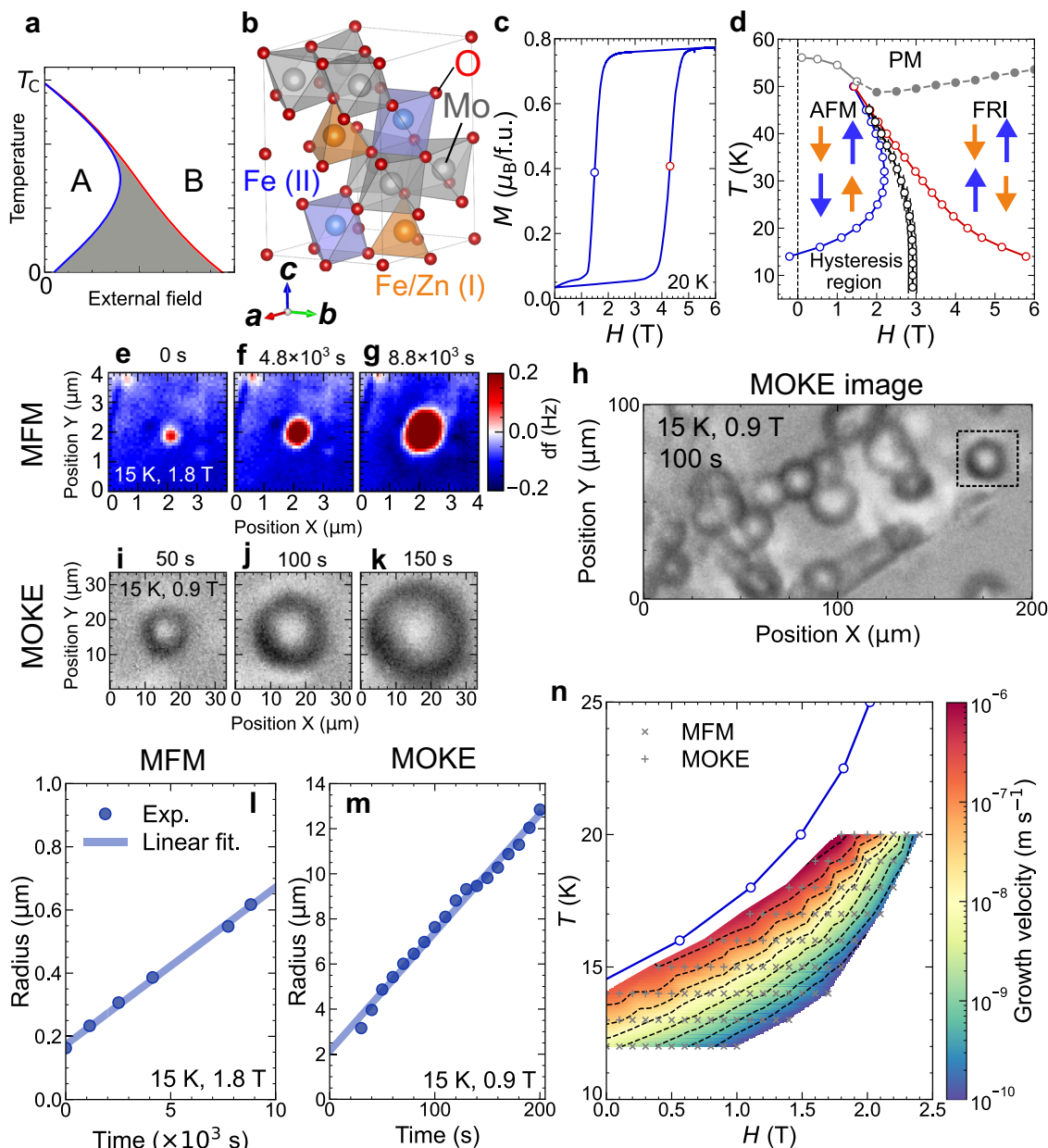
Among materials exhibiting low-temperature hysteresis broadening, we targeted  $(\text{Fe}_{0.95}\text{Zn}_{0.05})_2\text{Mo}_3\text{O}_8$  (Fig. 1b) because the hysteretic magnetic field-induced FOT is accessible with a moderate magnetic field<sup>24,25</sup>, as shown in the phase diagram (Fig. 1c, d); the FOT nature is confirmed by the fact that the extensive variables such as entropy and magnetization are discontinuous between the antiferromagnetic (AFM) and ferrimagnetic (FRI) phases and no critical phenomena are observed<sup>26</sup>. In  $(\text{Fe}_{1-y}\text{Zn}_y)_2\text{Mo}_3\text{O}_8$ , the magnetism originates from two crystallographically inequivalent  $\text{Fe}^{2+}$  (I) and  $\text{Fe}^{2+}$  (II) sites (Fig. 1b),

and  $\text{Mo}^{4+}$  layers have no contribution to the magnetism<sup>27</sup>. The magnetic moments of Fe(II) sites are slightly greater than those of Fe(I) sites<sup>24</sup>. In  $\text{Fe}_2\text{Mo}_3\text{O}_8$ , a metamagnetic transition occurs under magnetic fields along the *c*-axis<sup>25,28</sup>. In the low-field region, the two Fe(I) sites are antiferromagnetically ordered, and the same is true for the two Fe(II) sites, thus resulting in an antiferromagnetic (AFM) phase with no net macroscopic magnetization. When a sufficiently high magnetic field ( $\sim 7$  T) is applied, by contrast, the ferromagnetically aligned Fe(I) sites and the ferromagnetically aligned Fe(II) sites are antiferromagnetically ordered, thus resulting in a ferrimagnetic (FRI) phase with macroscopic magnetization. Doped Zn ions selectively occupy the Fe(I)-sites, which decreases the critical field of the metamagnetic transition<sup>29</sup> and causes the broadening of the hysteresis region at low temperatures<sup>25</sup>. For compositions above  $y=0.05$ , the FRI phase is so stable that the FRI to AFM transition can be observed only in a very narrow temperature-field region; on the other hand, for compositions below  $y=0.05$ , the AFM phase is so stable that the magnetic field-induced FOT is difficult to observe. For these reasons, this study focused on the composition of  $y=0.05$ , in which the transition field is well accessible, and thus experiments are feasible.

In this article, we show that the pronounced hysteresis broadening originates from an activated behavior of domain-wall dynamics as a function of both temperature and magnetic field, i.e., the creep motion of a domain wall. This is evidenced by real-space magnetic imaging experiments and numerical simulations. Furthermore, we also find that a sweep-rate-dependent magnetic hysteresis loop, which is important for understanding the performance under high-speed operation, is also well reproduced within our numerical simulations. The present study unveils a strong correlation between microscopic domain-wall motion and the macroscopic transition accompanied by low-temperature hysteresis broadening.

## Results and discussion

**Observation of an antiferromagnetic-domain growth.** To reveal the microscopic origin of the hysteresis broadening in  $(\text{Fe}_{0.95}\text{Zn}_{0.05})_2\text{Mo}_3\text{O}_8$  from the perspective of the nonequilibrium phase-evolution dynamics, we performed magnetic force microscopy (MFM) and magneto-optical Kerr effect (MOKE) imaging. In particular, we focused on AFM phase evolution in the matrix of the FRI phase, close to the lower-field boundary of the hysteresis region. To this end, a single-phase FRI state was first prepared by applying a magnetic field of 7 T at high temperature ( $\sim 25$  K), followed by field-cooling to a target temperature under 7 T. Then, the magnetic field was decreased to a target field, and the time evolution of the emergent AFM domain was measured while holding the temperature and magnetic field constant. Figure 1e–g shows the time evolution of the MFM images at 15 K and 1.8 T, noting that this comes from a magnetic signal (Supplementary Note 1). In the initial state, a small disk-shaped AFM domain was observed in the matrix of the FRI phase, and it gradually and continuously expanded over  $\sim 10^4$  s (Fig. 1f, g). A similar AFM domain was also observed at a different position. While MFM has a high spatial resolution of  $<50$  nm, image acquisition takes 10–20 min, and thus, rapid domain growth cannot be tracked. To track the faster motion of the AFM domain growth, we utilized MOKE imaging, which has a lower spatial resolution,  $\sim 1$   $\mu\text{m}$ , but a faster image acquisition time, i.e., 1 s. In MOKE imaging, the AFM domains were observed as similar multiple circular spots with dark boundaries in a much wider field of view (Fig. 1h). Note that images shown in Fig. 1h–k are divided by the raw MOKE image at 0 s to remove the influence of the position-dependent intensity of the incident light. Figure 1i–k



**Fig. 1** Low-temperature hysteresis broadening and growth of the AFM domain in  $(\text{Fe}_{1-y}\text{Zn}_y)_2\text{Mo}_3\text{O}_8$ . **a** Archetypal phase diagram of a field-induced first-order phase transition (FOT) between two competing phases (labeled by A and B) with different symmetries. The solid lines in **(a)** represent magnetic fields at which the phase transition is observed during magnetic field sweeps at a given rate. Such hysteresis broadening is not always but is frequently observed in a field-induced FOT between competing phases. **b** The crystal structure of  $(\text{Fe}_{1-y}\text{Zn}_y)_2\text{Mo}_3\text{O}_8$ .  $\text{Fe}^{2+}$  ions at the Fe(I)-sites (brown) and Fe(II)-sites (blue) are surrounded by oxygen tetrahedra and octahedra, respectively.  $\text{Mo}^{4+}$  ions (gray) form the nonmagnetic spin-trimer. **c** Isothermal magnetization curve of  $(\text{Fe}_{0.95}\text{Zn}_{0.05})_2\text{Mo}_3\text{O}_8$  at 20 K. Blue (red) open circles indicate the transition fields from the FRI to AFM (AFM to FRI) phases, where AFM and FRI represent antiferromagnetic and ferrimagnetic, respectively. These transition fields are defined as the inflection points of  $M$ - $H$  curves. **d** Temperature-magnetic field phase diagram of  $(\text{Fe}_{0.95}\text{Zn}_{0.05})_2\text{Mo}_3\text{O}_8$ . The transitions from the AFM to FRI phases and from the FRI to the AFM phases are indicated by red and blue open circles, respectively. Black open circles with error bars represent the equilibrium FOT phase boundary, taken from ref. <sup>26</sup>. Orange and blue arrows in the schematic represent spins at Fe(I) and Fe(II) sites, respectively. **e-g** Magnetic force microscopy (MFM) images of a time-evolving AFM domain at 15 K and 1.8 T at **e** 0 s, **f**  $4.8 \times 10^3$  s and **g**  $8.8 \times 10^3$  s. **h** Magneto-optical-Kerr effect-microscopy (MOKE) image of a wider area at (15 K, 0.9 T). **i-k** MOKE images of a time-evolving AFM domain at (15 K, 0.9 T) indicated by the dotted rectangle in **(h)** at **i** 50 s, **j** 100 s and **k** 150 s. Images shown in **(h-k)** are divided by the raw MOKE image at 0 s to remove the influence of the position-dependent intensity of the incident light. **l, m** Time dependences of a radius at **l** (15 K, 1.8 T) and **m** (15 K, 0.9 T). **n** Contour map of the growth velocity, superimposed on the phase diagram. The blue solid line with blue open circles indicates the transitions from the FRI to AFM phases on a field-decreasing process. The black dashed lines on the contour map represent contour lines drawn at 1 and 3 series from  $1.0 \times 10^{-10}$  to  $1.0 \times 10^{-6}$  in logarithmic representation. Gray cross and plus marks represent the points measured with MFM and MOKE, respectively.

displays the AFM domain growth at 15 K and 0.9 T, demonstrating that compared with the data at a higher magnetic field (Fig. 1e–g), the growth speed of the AFM domains is pronouncedly faster.

We found that the radius of the circular AFM domain changes almost linearly with respect to elapsed time, as shown in Fig. 1l, m, and from this behavior, a constant growth velocity,  $v$ , of the AFM domain was defined as the slope of this plot; the time evolution of the circular domain appears monotonic, suggesting that the spatial distribution of impurities can be regarded as homogenous as far as the present domain-wall dynamics are concerned. The same analysis was performed for various temperatures,  $T$ , and magnetic fields,  $H$ , and thus we were successful in deriving  $v(H, T)$  for  $T \leq 20$  K: Above this temperature, the image contrast significantly decreased, although the reason is not clear; therefore, the analysis was not possible. The results are summarized as a contour plot of the growth velocity in Fig. 1n (see also Supplementary Note 2 for the reproducibility at different positions), and to gain insight into the relationship between  $v(H, T)$  and the hysteresis line  $H_{\text{low}}^*(T)$ , the contour plot is superimposed on the phase diagram. Here, two important points can be highlighted. On the one hand, the curvature of the contour line is similar to that of the  $H_{\text{low}}^*(T)$  line, suggesting that the profile of the hysteresis line is closely related to the microscopic growth process of the AFM domain. On the other hand, although the growth speed near the  $H_{\text{low}}^*(T)$  line is expected to have a particularly important impact on the macroscopic phase evolution under the continuous field-sweeping experiments, the information was not obtained from the above analysis because the growth speed is far beyond the detection limit,  $\sim 1 \mu\text{m s}^{-1}$ .

**Creep motion of a domain wall between the antiferromagnetic and ferrimagnetic phases.** To obtain  $v(H, T)$  near the  $H_{\text{low}}^*(T)$  line, the microscopic mechanism should be identified together with the corresponding formula. To this end, below we consider the application of the so-called modified Merz's law that describes the creep motion of an elastic interface, such as a domain wall (DW), in a disordered medium<sup>30–32</sup>. The characteristic of the modified Merz's law is that the velocity of a moving DW obeys activated behavior with respect to both temperature,  $T$ , and the driving force exerted on the DW,  $F$ . The equation is given as  $v(T, F) = A^* \exp[-\Delta/(TF^\mu)]$ , where  $\mu$  is a so-called dynamical exponent and  $A$  and  $\Delta$  represent the limit of high speed and temperature-force-composite activation barrier, respectively. When applying this equation to  $(\text{Fe}_{1-y}\text{Zn}_y)_2\text{Mo}_3\text{O}_8$ , the driving force should be measured with reference to  $H_c(T)$  (for more details, see Supplementary Note 3), which has recently been determined by making full use of the thermodynamic relations<sup>26</sup> as indicated by white circles in Fig. 1d. Thus, in the present case, the modified Merz's law is given as

$$v(T, \delta H) = A \exp\left[-\frac{\Delta}{T \times (\delta H)^\mu}\right], \quad (1)$$

where  $\delta H(T) = |H(T) - H_c(T)|$ . Equation (1) describes the average velocity of the creep motion rather than the instantaneous velocity that may be affected by the details of the spatial distribution of impurities.

Figure 2a displays the growth velocities at various temperatures, plotted against  $1/(\delta H)^\mu$ . We find that the observed velocities are well reproduced by Eq. (1) (solid lines, Fig. 2a), indicating that the observed DW motion should be dictated by the creep motion. We note, however, that it is not so obvious to what extent the creep motion describes the actual DW dynamics outside the examined parameter region; in fact, previous

theoretical studies predict that the DW dynamics change from the creep to flow regimes as the driving force increases<sup>31</sup>. We will discuss this issue later. The optimized adjustable parameters are  $A = 3806.5 \text{ (m s}^{-1}\text{)}$ , which is quite close to the expected velocity of the acoustic phonon in  $\text{Fe}_2\text{Mo}_3\text{O}_8$ ,  $2.7\text{--}6.6 \times 10^3 \text{ m s}^{-1}$  calculated from the elastic constants<sup>33</sup>, and  $\mu = 0.4$ . The similarity between the value of  $A$  and the phonon velocity may imply that structural change accompanies the metamagnetic transition and thus affects the dynamics of DW. The value of  $\Delta$  is nearly constant ( $\sim 500$ ) within the measured temperature range (Fig. 2b), and the residual weak temperature dependence may be attributed to that of the order parameter. In ferroic materials, it is known that the value of  $\mu$  depends on both the dimensionality of the DW and the type of disorder, which is generally classified into random-bond or random-field types<sup>31,34,35</sup>. However, for the case of DWs separating distinct symmetry phases, such as AFM and FRI, such classification of disorder is not straightforward (for details, see Supplementary Note 4). Thus, although  $\mu = 0.4$  appears to be close to  $\mu = 0.5\text{--}0.6$ , which is a value reported for two-dimensional DWs under the influence of random-bond-type disorder<sup>32,36</sup>, its implications are not clear.

**Origin of the pronounced hysteresis broadening.** Nevertheless, having established that Eq. (1) reproduces the observed  $v(T, \delta H)$  well, we can supplement the data near the  $H_{\text{low}}^*(T)$  line by the extrapolation according to Eq. (1), enabling us to quantitatively investigate the relationship between the creep-like growth velocity and the pronounced hysteresis broadening. To this end, we use the Kolmogorov–Avrami–Ishibashi (KAI) model<sup>37,38</sup>, which can calculate the volume fraction of a growing domain for a given DW velocity while avoiding the complexity caused by domain coalescence (Fig. 3a). Given that in the present observation, the nucleation sites are always at the same positions, we applied the formalism of the KAI model with the so-called one-step nucleation mechanism (for details, see Supplementary Note 5):

$$c(t) = 1 - \exp[-NS(t)], \quad (2)$$

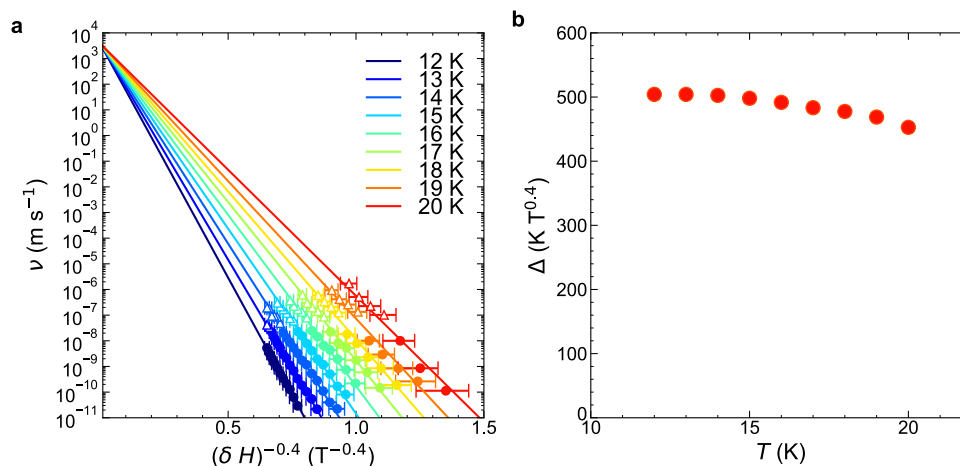
where  $c(t)$ ,  $N$ , and  $S(t)$  are the time-dependent volume fraction of the AFM domain, the density of nucleation sites, and the time ( $t$ )-dependent extended area caused by a single-nucleation site, respectively. When calculating  $S(t)$ , the DW velocity should be integrated with respect to  $t$ : In the present study, because a phase transition under continuous field-sweeping experiments is considered, the DW velocity is time-dependent via the time-dependent driving force,  $\delta H(t)$ . Thus,  $c(t)$  is formulated as follows:

$$c(t) = 1 - \exp\left[-N \times \alpha(n) \times \left\{\int_0^t v(T, \delta H(s)) ds\right\}^n\right], \quad (3)$$

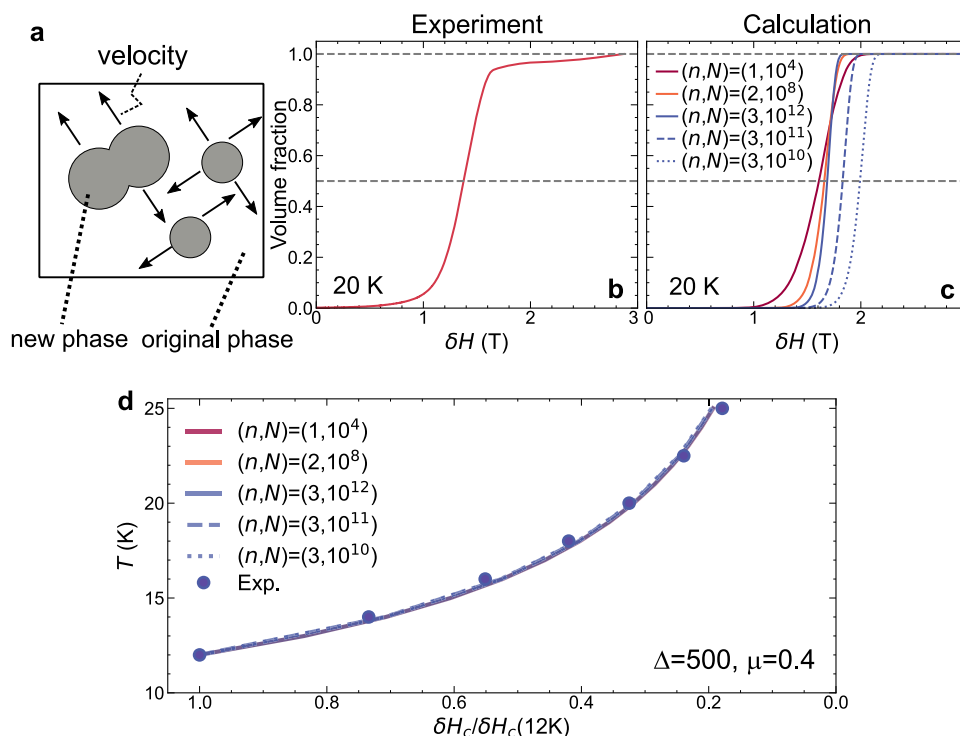
where  $\alpha(n)$  is a shape factor and equal to 2,  $\pi$ , or  $4\pi/3$  depending on stripe domain growth (one dimensional,  $n = 1$ ), circular domain growth (two dimensional,  $n = 2$ ), or spherical domain growth (three dimensional,  $n = 3$ ), respectively.

The calculation of the phase evolution was performed by using the experimentally obtained parameter set,  $A = 3806.5$ ,  $\mu = 0.4$ , and  $\Delta = 500$ . We define the transition field  $\delta H_c(T)$  as the field at which the phase evolution is half complete. The experimental transition profile at 20 K and the corresponding calculated results are shown in Fig. 3b, c, respectively. The details of the transition profile, such as the value of  $\delta H_c(T)$  and the sharpness of the transition, depend on  $N$  and  $n$  (Fig. 3c). However, we find that the shape of the hysteresis line is not sensitive to  $N$  and  $n$  (Fig. 3d and Supplementary Fig. 4a, b). Therefore, upon comparing the hysteresis line profiles of the calculation and experiments, the normalized temperature dependence of  $\delta H_c(T)/\delta H_c(12 \text{ K})$  is





**Fig. 2** The fitting of growth velocities of an antiferromagnetic domain with Merz's law. **a** Growth velocities plotted against the inverse of the driving magnetic field. The data indicated by filled circles and open triangles are obtained from the MFM and MOKE experiments, respectively. The solid lines represent the fitting with  $v(T, \delta H) = A \exp[-\frac{\Delta}{T \times (\delta H)^\mu}]$  with  $\mu = 0.4$ , where  $\delta H$  represents the driving force of the phase transition and it is given by  $H - H_0$  with  $H_0$  being the equilibrium FOT phase boundary. The error bars of the data points originate from the error bars of the thermodynamic phase boundary displayed in Fig. 1d. **b** Temperature dependence of the activation energy  $\Delta$  in Eq. (1), obtained from the fitting in (a).

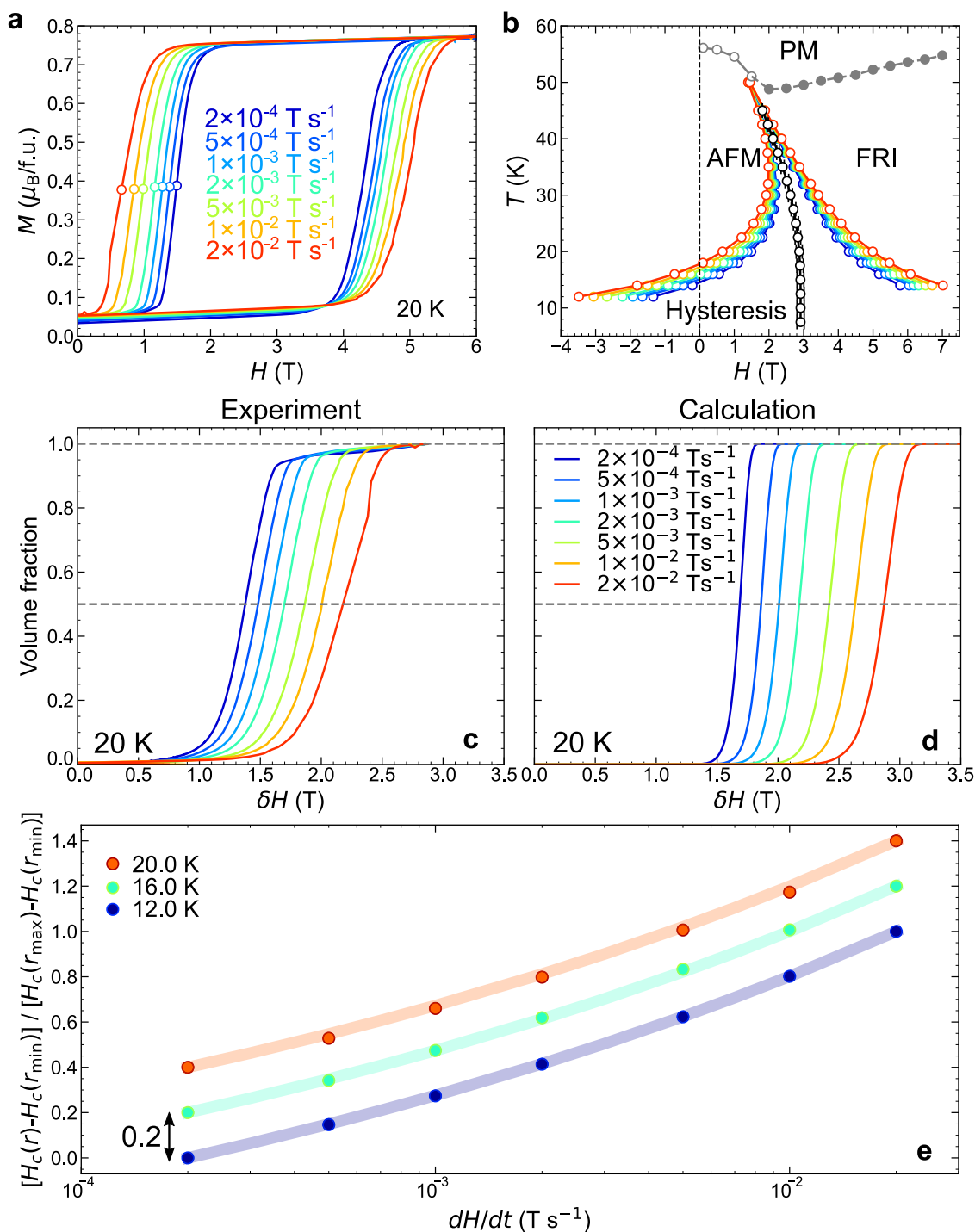


**Fig. 3** Calculation of the low-temperature hysteresis broadening based on the Kolmogorov-Avrami-Ishibashi (KAI) model combined with modified Merz's law. **a** Schematic illustration of the KAI model for a two-dimensional case. Gray regions represent nuclei of a new phase, which are isotropically growing. **b, c** The experimental (b) and corresponding calculated (c) transition profiles at 20 K. The vertical axis in (b) represents the volume fraction that is calculated as  $[M(7\text{ T}) - M(H)] / [M(7\text{ T}) - M(0\text{ T})]$ , where  $M(H)$  is magnetization. The horizontal axis is  $\delta H(T) = |H(T) - H_c(T)|$ . The calculation was performed following Eq. (3) at selected values of  $(n, N)$ , where  $n$  and  $N$  represent the system dimension and the density of the nucleation sites, respectively. **d** Comparison of the transition fields from the FRI to AFM phases, obtained from the calculation and experiments. The transition fields are normalized by the transition field at 12 K. The experimental and simulated data are represented by the filled circles and curves, respectively.

the quantity that should be considered. The comparison is displayed in Fig. 3d, showing good agreement with the experiment. Furthermore, the profile of the hysteresis broadening is less pronounced for a higher  $\mu$  value, such as  $\mu = 1$  (Supplementary Note 5), which is a value reported for DWs in ferroic materials with random-field type disorder<sup>32,39,40</sup>. These

observations indicate that the peculiar  $T$  and  $\delta H$  dependences of the DW creep velocity, underpinned by a low  $\mu$  value, are at the heart of the pronounced hysteresis broadening.

**Sweep-rate dependence.** Finally, to further corroborate the relationship between the creep dynamics of the DWs and the



**Fig. 4 Sweep-rate-dependent behavior of the hysteresis lines.** **a** Isothermal magnetization curves at 20 K measured at various sweep rates, obtained in the experiments. **b** The transition lines determined by various sweep rates. Open circles represent the sweep-rate-dependent transition fields from FRI (AFM) to AFM (FRI) phases, determined by isothermal magnetization curve measurements. **c, d** The experimental (c) and corresponding calculated (d) sweep-rate-dependent transition profiles at 20 K. The definitions of the vertical and horizontal axes are the same as in Fig. 3b, c. **e** Comparison of the sweep-rate-dependent transition fields from the FRI to the AFM phases at selected temperatures, obtained from the calculation and the experiments. The transition fields are normalized as  $[\delta H_c(r) - \delta H_c(r_{\min})] / [\delta H_c(r_{\max}) - \delta H_c(r_{\min})]$  at the lowest and highest sweep rates, i.e.,  $r_{\min} = 2 \times 10^{-4} \text{ T s}^{-1}$  and  $r_{\max} = 2 \times 10^{-2} \text{ T s}^{-1}$ . The experimental and simulated data are represented by the filled circles and curves, respectively. Each curve is shifted by 0.2 for visibility.

pronounced hysteresis broadening, it would be important to test another aspect of the hysteresis line, that is, the sweep-rate dependence. If the  $H_{\text{low}}^*(T)$  line is dictated by the creep dynamics, the  $H_{\text{low}}^*(T)$  line should depend on the sweep rate as a natural consequence of the kinetic aspect. Figure 4a shows the

sweep-rate dependences of the isothermal magnetization curves at 20 K, and it can be seen that the FRI-AFM transition field (white circles) appreciably decreases as the sweep rate increases. This feature is conspicuous especially below 30 K (Fig. 4b), highlighting the kinetic aspect of the FOT process. Using the KAI

model, the field-induced transition at various field-sweeping rates at 20 K can be calculated and compared with experimental results (Fig. 4c, d). As in the case of the temperature dependence of the hysteresis line, we find that the normalized sweep-rate dependence  $[\delta H_c(r) - \delta H_c(r_{\min})]/[\delta H_c(r_{\max}) - \delta H_c(r_{\min})]$  depends on  $N$  and  $n$  only weakly. We therefore compare this value between the experiments and calculations at selected temperatures, as shown in Fig. 4e (see also Supplementary Fig. 4d–f), confirming that the sweep-rate dependence of the transition field is successfully captured by the calculation at a quantitative level.

**Conclusion.** The present analysis relies on extrapolating the  $v(T, \delta H)$  data toward  $H_{\text{low}}$  within the framework of the modified Merz's law (Eq. (1)), and thus, the validity of the model near  $H_{\text{low}}$  may not be necessarily clear. However, we have demonstrated that the two main characteristics of the hysteresis line at low temperatures, that is, the pronounced broadening and the pronounced sweep-rate dependence are both quantitatively explained by considering the creep motion of the DW obeying an activated form with respect to temperature and magnetic field. These observations indicate that the modified Merz's law still captures the DW dynamics near  $H_{\text{low}}$ . Given that not all FOT materials exhibit pronounced hysteresis broadening, the DW creep dynamics, including the  $\mu$  value, are likely to vary widely from material to material. So far, DW dynamics has been investigated exclusively in ferroic systems because of their importance in applications. Toward exotic applications based on an FOT beyond ferroic systems, our findings suggest that control of  $\mu$  in a phase-competing system is likely a key ingredient.

## Methods

**Crystal growth.** Single crystals of  $(\text{Fe}_{0.95}\text{Zn}_{0.05})_2\text{Mo}_3\text{O}_8$  were grown by chemical vapor transport reaction method following the literature<sup>24,25,41</sup>. Powders of  $\text{MoO}_3$ ,  $\text{Fe}$ ,  $\text{Fe}_2\text{O}_3$ , and  $\text{ZnO}$  were mixed and ground in the stoichiometric molecular ratio. The powder was sealed in the inner quartz tube (diameter 15 mm, length 130 mm) together with 100 mg of  $\text{TeCl}_4$  as the transport agent. This ampoule was double-sealed with the outer quartz tube (diameter 20 mm, length 200 mm), and placed in a three-zone furnace. After 24 h of back transport (845 °C on the precursor-loaded side; 980 °C on the growth side), the temperature gradient was reverted to be 980 °C for the load side and 845 °C for the growth side, and maintained for 11 days.

**Magnetization measurement.** Magnetization was measured by reciprocating sample option (RSO) and vibrating sample magnetometer (VSM) modes in a commercial superconducting quantum interference device magnetometer (MPMS-XL and MPMS-3; Quantum Design). Magnetic sweeping rates from  $2 \times 10^{-4} \text{ T s}^{-1}$  to  $2 \times 10^{-2} \text{ T s}^{-1}$  were controlled in MPMS-3 and the VSM measurement was performed in the continuous sampling mode.

**Magnetic force microscopy measurement.** Frequency-modulated MFM was performed under high vacuum conditions with a commercially available scanning probe microscope (atto-cube AFM/MFM I). We used the MFMR tip (supplied by NANOSENSORS) with a tip radius of  $\sim 50 \text{ nm}$ . The typical sample dimension was  $\sim 3.0 \times 2.0 \times 1.0 \text{ mm}^3$  with a mass of 31.95 mg. We prepared a sample with a naturally grown surface that is normal to the  $c$ -axis. Gold with a thickness of 50–100 nm was deposited on the surface to avoid the charge-up problem during the measurement. The MFM measurement was performed in noncontact mode with a lift height of 100–200 nm. The amplitude of the cantilever oscillation was approximately 10–

20 nm. The resonant frequency was  $\approx 63.6 \text{ kHz}$ , and the Q-factor was  $\approx 3.5 \times 10^4$  under the measurement conditions.

**Magneto-optical Kerr effect (MOKE) measurement.** MOKE measurement setup follows the literature<sup>42</sup>. A commercial polarizing microscope (BAXFM, Olympus) was fixed to the aluminum frame self-constructed above the physical property measurement system (PPMS; PPMS-14T, Quantum Design). An infinity-corrected objective lens (PLN4XP, Olympus) attached to a fiberglass-reinforced plastic tube (diameter 16 mm, length 1 m) was inserted into the sample chamber of PPMS. Light from a LED source (625 nm, M624L4-C1, Thorlabs) passed through a polarizer and coaxially illuminated onto the sample. Reflected light through the objective lens, an analyzer, and a television (TV) lens (magnification of  $\times 5$ ) was captured by a CMOS camera (PCO). The polarization is shifted about  $5^\circ$  from the orthogonal configuration<sup>42</sup>. The temperature and magnetic field were controlled by the PPMS control system. The sample on the sapphire plate was placed on the PPMS sample puck (P101/3 A) with varnish and installed into the sample chamber of PPMS. The measurement was performed with the naturally grown surface of the same sample used in the MFM measurement.

## Data availability

The data are available from the corresponding authors upon reasonable request.

## Code availability

The source codes are available from the corresponding authors upon reasonable request.

Received: 25 July 2023; Accepted: 31 August 2023;

Published online: 13 September 2023

## References

1. Coey, J. M. D. Hard magnetic materials: a perspective. *IEEE Trans. Magn.* **47**, 4671 (2011).
2. Damjanovic, D. Ferroelectric, dielectric and piezoelectric properties of ferroelectric thin films and ceramics. *Rep. Prog. Phys.* **61**, 1267 (1998).
3. Piramanayagam, S. N. Perpendicular recording media for hard disk drives. *J. Appl. Phys.* **102**, 011301 (2007).
4. Dawber, M., Rabe, K. M. & Scott, J. F. Physics of thin-film ferroelectric oxides. *Rev. Mod. Phys.* **77**, 1083 (2005).
5. Silveyra, J. M., Ferrara, E., Huber, D. L. & Monson, T. C. Soft magnetic materials for a sustainable and electrified world. *Science* **362**, ea00195 (2018).
6. Tokura, Y. Critical features of colossal magnetoresistive manganites. *Rep. Prog. Phys.* **69**, 797 (2006).
7. Matsuura, K. et al. Kinetic pathway facilitated by a phase competition to achieve a metastable electronic phase. *Phys. Rev. B* **103**, L041106 (2021).
8. Hou, H., Qian, S. & Takeuchi, I. Materials, physics and systems for multicaloric cooling. *Nat. Rev. Mat.* **7**, 633 (2022).
9. Quach, D.-T. et al. Minor hysteresis patterns with a rounded/sharpened reversing behavior in ferromagnetic multilayer. *Sci. Rep.* **8**, 4461 (2018).
10. Wu, W. et al. Formation of pancakelike ising domains and giant magnetic coercivity in ferrimagnetic  $\text{LuFe}_2\text{O}_4$ . *Phys. Rev. Lett.* **101**, 137203 (2008).
11. Roy, S. B. et al. Devitrification of the low temperature magnetic-glass state in  $\text{Gd}_5\text{Ge}_4$ . *Phys. Rev. B* **75**, 184410 (2007).
12. Fujieda, S., Fukamichi, K. & Suzuki, S. Itinerant-electron metamagnetic transition in  $\text{LaFe}_2\text{B}_6$ . *J. Magn. Magn. Mater.* **421**, 403 (2017).
13. Manekar, M. A. et al. First-order transition from antiferromagnetism to ferromagnetism in  $\text{Ce}(\text{Fe}_{0.96}\text{Al}_{0.04})_2$ . *Phys. Rev. B* **64**, 104416 (2001).
14. Kushwaha, P., Rawat, R. & Chaddah, P. Metastability in the ferrimagnetic–antiferromagnetic phase transition in Co substituted  $\text{Mn}_2\text{Sb}$ . *J. Phys. Condens. Matter.* **20**, 022204 (2008).
15. Singh, V., Karmakar, S., Rawat, R. & Kushwaha, P. Giant negative magnetoresistance and kinetic arrest of first-order ferrimagnetic–antiferromagnetic transition in Ge doped  $\text{Mn}_2\text{Sb}$ . *J. Appl. Phys.* **125**, 233906 (2019).

16. Umetsu, R. Y. et al. Magnetoresistance and transformation hysteresis in the  $\text{Ni}_{50}\text{Mn}_{34.4}\text{In}_{15.6}$  metamagnetic shape memory alloy. *Mater. Trans.* **54**, 291 (2013).
17. Niitsu, K., Date, H. & Kainuma, R. Thermal activation of stress-induced martensitic transformation in Ni-rich Ti-Ni alloys. *Scr. Mater.* **186**, 263 (2020).
18. Suzuki, Y. Direct observation of reversible liquid-liquid transition in a trehalose aqueous solution. *Proc. Natl. Acad. Sci. USA* **119**, e2113411119 (2022).
19. Gaunt, P. Ferromagnetic domain wall pinning by a random array of inhomogeneities. *Philos. Mag. B* **48**, 261 (1983).
20. Cai, J.-W., Okamoto, S., Kitakami, O. & Shimada, Y. Large coercivity and surface anisotropy in MgO/Co multilayer films. *Phys. Rev. B* **63**, 104418 (2001).
21. Morosan, E. Z. et al. Sharp switching of the magnetization in  $\text{Fe}_{1/4}\text{TaS}_2$ . *Phys. Rev. B* **75**, 104401 (2007).
22. Kagawa, F. & Oike, H. Quenching of charge and spin degrees of freedom in condensed matter. *Adv. Mater.* **29**, 1601979 (2017).
23. Oike, H., Kamitani, M., Tokura, Y. & Kagawa, F. Kinetic approach to superconductivity hidden behind a competing order. *Sci. Adv.* **4**, eaau3489 (2018).
24. Bertrand, D. & Kerner-Czeskleba, H. Étude structurale et magnétique de molybdates d'éléments de transition. *J. Phys.* **36**, 379 (1975).
25. Kurumaji, T., Ishiwata, S. & Tokura, Y. Doping-tunable ferrimagnetic phase with large linear magnetoelectric effect in a polar magnet  $\text{Fe}_2\text{Mo}_3\text{O}_8$ . *Phys. Rev. X* **5**, 031034 (2015).
26. Matsuura, K. et al. Thermodynamic determination of the equilibrium first-order phase-transition line hidden by hysteresis in a phase diagram. *Sci. Rep.* **13**, 6876 (2023).
27. Cotton, F. A. Metal atom clusters in oxide systems. *Inorg. Chem.* **3**, 1217 (1964).
28. Wang, Y. et al. Unveiling hidden ferrimagnetism and giant magnetoelectricity in polar magnet  $\text{Fe}_2\text{Mo}_3\text{O}_8$ . *Sci. Rep.* **5**, 12268 (2015).
29. Varret, F., Czeskleba, H., Hartmann-Boutron, F. & Imbert, P. Étude par effet Mössbauer de l'ion  $\text{Fe}^{2+}$  en symétrie trigonale dans les composés du type  $(\text{Fe}, \text{M})_2\text{Mo}_3\text{O}_8$  ( $\text{M} = \text{Mg}, \text{Zn}, \text{Mn}, \text{Co}, \text{Ni}$ ) et propriétés magnétiques de  $(\text{Fe}, \text{Zn})_2\text{Mo}_3\text{O}_8$ . *J. Phys.* **33**, 549 (1972).
30. Merz, W. J. Domain Formation and domain wall motions in ferroelectric  $\text{BaTiO}_3$  single crystals. *Phys. Rev.* **95**, 690 (1954).
31. Chauve, P., Giamarchi, T. & Doussal, P. L. Creep and depinning in disordered media. *Phys. Rev. B* **62**, 6241 (2000).
32. Kleemann, W. Universal domain wall dynamics in disordered ferroic materials. *Ann. Rev. Mater. Res.* **37**, 415 (2007).
33. Jain, A. et al. Commentary: The Materials Project: a materials genome approach to accelerating materials innovation. *APL Mater.* **1**, 011002 (2013). **Data retrieved from the Materials Project for  $\text{Fe}_2\text{Mo}_3\text{O}_8$  (mp-504974) from database version v2022.10.28.**
34. Nattermann, T., Shapir, Y. & Vilfan, I. I. Interface pinning and dynamics in random systems. *Phys. Rev. B* **42**, 8577 (1990).
35. Huse, D. A. & Henley, C. L. Pinning and roughening of domain walls in Ising systems due to random impurities. *Phys. Rev. Lett.* **54**, 2708 (1985).
36. Lemerle, S. et al. Domain wall creep in an Ising ultrathin magnetic film. *Phys. Rev. Lett.* **80**, 849 (1998).
37. Avrami, M. Kinetics of phase change. I general theory. *Chem. Phys.* **7**, 1103 (1939).
38. Ishibashi, Y. & Takagi, Y. Note on ferroelectric domain switching. *J. Phys. Soc. Jpn.* **31**, 506 (1971).
39. Tybell, T., Paruch, P., Giamarchi, T. & Triscone, J. M. Domain wall creep in epitaxial ferroelectric  $\text{Pb}(\text{Zr}_{0.2}\text{Ti}_{0.08})\text{O}_3$  thin films. *Phys. Rev. Lett.* **89**, 097601 (2002).
40. Jo, J. Y. et al. Nonlinear dynamics of domain-wall propagation in epitaxial ferroelectric thin films. *Phys. Rev. Lett.* **102**, 045701 (2009).
41. Strobel, P., Le Page, Y. & McAlister, S. Growth and physical properties of single crystals of  $\text{Fe}^{\text{II}}\text{Mo}^{\text{IV}}\text{O}_8$ . *J. Solid State Chem.* **42**, 242 (1982).
42. Kinoshita, Y., Miyakawa, T., Xu, X. & Tokunaga, M. Long-distance polarizing microscope system combined with solenoid-type magnet for microscopy and simultaneous measurement of physical parameters. *Rev. Sci. Instrum.* **93**, 073702 (2022).
43. Momma, K. & Izumi, F. VESTA 3 for three-dimensional visualization of crystal, volumetric and morphology data. *J. Appl. Crystallogr.* **44**, 1272 (2011).

### Acknowledgements

This work was supported by JSPS KAKENHI (Grant No. 21K14398, No. 21H04442, and No. 18H05225, No. 22H01164, and No. 23H04862), JST PRESTO (No. JPMJPR21Q2) and JST CREST (No. JPMJCR1874). K.M. was supported by the Special Postdoctoral Researcher Program of RIKEN. The crystal structure was visualized by VESTA 3<sup>43</sup>.

### Author contributions

K.M. and F.K. planned the project. K.M. and Y.N. performed the magnetization measurement and the magnetic force microscopy measurement, and analyzed the data. K.M. and Y.K. performed the MOKE experiment, and K.M. analyzed the data. T.K. synthesized the single crystals used for this study. K.M. performed the KAI model calculation. K.M. and F.K. wrote the manuscript. K.M., Y.N., Y.K., T.K., A.M., H.O., M.T., Y.T., and F.K. discussed the results and commented on the manuscript.

### Competing interests

The authors declare no competing interests.

### Additional information


**Supplementary information** The online version contains supplementary material available at <https://doi.org/10.1038/s43246-023-00399-8>.

**Correspondence** and requests for materials should be addressed to Keisuke Matsuura or Fumitaka Kagawa.

**Peer review information** *Communications Materials* thanks Dong-Hyun Kim and the other, anonymous, reviewer(s) for their contribution to the peer review of this work. Primary Handling Editors: Aldo Isidori and John Plummer.

**Reprints and permission information** is available at <http://www.nature.com/reprints>

**Publisher's note** Springer Nature remains neutral with regard to jurisdictional claims in published maps and institutional affiliations.

 **Open Access** This article is licensed under a Creative Commons Attribution 4.0 International License, which permits use, sharing, adaptation, distribution and reproduction in any medium or format, as long as you give appropriate credit to the original author(s) and the source, provide a link to the Creative Commons license, and indicate if changes were made. The images or other third party material in this article are included in the article's Creative Commons license, unless indicated otherwise in a credit line to the material. If material is not included in the article's Creative Commons license and your intended use is not permitted by statutory regulation or exceeds the permitted use, you will need to obtain permission directly from the copyright holder. To view a copy of this license, visit <http://creativecommons.org/licenses/by/4.0/>.

© The Author(s) 2023